Imaging spin-wave damping underneath metals using electron spins in diamond

Bertelli, I.; Simon, B.G.; Yu, T.; Aarts, J.; Bauer, G.E.W.; Blanter, Y.M.; Sar, T. van der

ADVANCED QUANTUM TECHNOLOGIES
www.advquantumtech.com

Imaging Spin-Wave Damping Underneath Metals Using Electron Spins in Diamond

*Iacopo Bertelli, Brecht G. Simon, Tao Yu, Jan Aarts, Gerrit E. W. Bauer, Yaroslav M. Blanter, and Toeno van der Sar**

Spin waves in magnetic insulators are low-damping signal carriers that can enable a new generation of spintronic devices. The excitation, control, and detection of spin waves by metal electrodes is crucial for interfacing these devices to electrical circuits. As such, it is important to understand metal-induced damping of spin-wave transport, but characterizing this process requires access to the underlying magnetic films. Here it is shown that electronic sensor spins in diamond enable imaging of spin waves that propagate underneath metals in magnetic insulators. This capability is then used to reveal a 100-fold metal-induced increase in spin-wave damping. The damping enhancement is attributed to spin-wave-induced electrical currents as well as, above a certain frequency, three-magnon scattering processes. This interpretation is supported by deriving expressions for the current-induced damping and the three-magnon threshold from the Landau–Lifshitz–Gilbert equation that agree well with the observations. The detection of buried scattering centers further highlights the technique's power for assessing spintronic device quality. These results open new avenues for studying metal – spin-wave interactions and provide access to interfacial processes such as spin-wave injection via the spin-Hall effect.

1. Introduction

Spin waves are collective, wave-like excitations of the spins in magnetic materials.[1] The field of magnon spintronics aims at using these waves as signal carriers in information processing devices.[2] Since its recent inception, the field has matured rapidly[3] and successfully realized prototypical spin-wave devices that implement logical operations.[4–8] In such devices, the spin waves are typically excited inductively[4–8] or via spin-pumping based on the spin-Hall effect,[9,10] using electric currents in metal electrodes that are deposited on top of thin-film magnetic insulators. It is a key challenge to understand the interaction between metals and spin waves in magnetic insulators, but this requires access to the buried magnetic films and is hampered by the opacity of the metals to optical probes.

We address this challenge using magnetic imaging based on electron spins in diamond.[11] Metal films of sub-skindepth thickness are transparent for microwave magnetic fields, which enables imaging of spin waves traveling underneath the metals by detecting their magnetic stray fields. We demonstrate this ability by imaging spin waves that travel underneath 200-nm-thick metal electrodes in a thin film of the magnetic insulator yttrium iron garnet (YIG). We find that the spatial spin-wave profiles under the metals reveal a surprisingly strong metal-induced spin-wave damping. By introducing the spin-wave-induced currents in the metal self-consistently into the Landau–Lifshitz–Gilbert (LLG) equation, we derive an analytical expression for the spin wave damping that matches our experimental observations without free parameters. We demonstrate that this

I. Bertelli, B. G. Simon, G. E. W. Bauer, Y. M. Blanter, T. van der Sar
Department of Quantum Nanoscience
Kavli Institute of Nanoscience
Delft University of Technology
Lorentzweg 1, Delft 2628 CJ, The Netherlands
E-mail: t.vandersar@tudelft.nl

The ORCID identification number(s) for the author(s) of this article can be found under https://doi.org/10.1002/qute.202100094

DOI: 10.1002/qute.202100094

I. Bertelli, J. Aarts
Huygens – Kamerlingh Onnes Laboratorium
Leiden University
Niels Bohrweg 2, Leiden 2300 RA, The Netherlands

T. Yu
Max Planck Institute for the Structure and Dynamics of Matter
Luruper Chausee 149, Hamburg 22761, Germany

T. Yu
School of Physics
Huazhong University of Science and Technology
Wuhan 430074, China

G. E. W. Bauer, Y. M. Blanter
WPI-AIMR & Institute for Materials Research & CSRN
Tohoku University
Sendai 980–8577, Japan

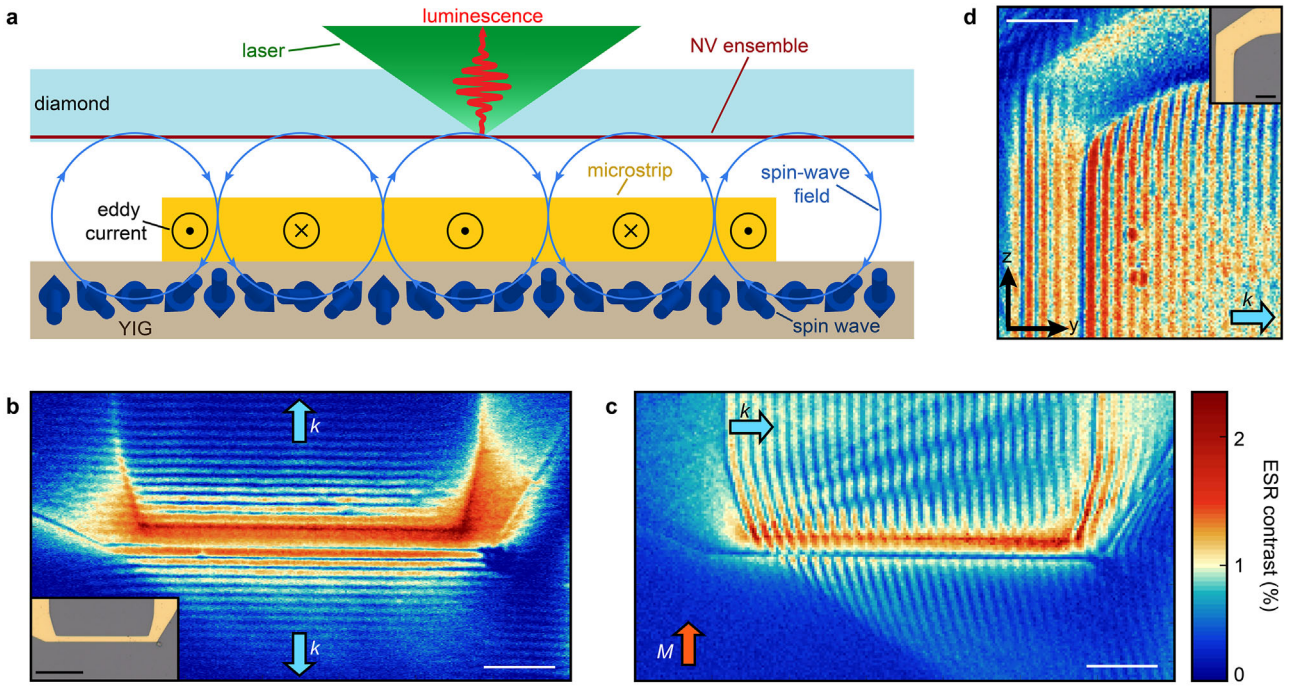

Figure 1. Magnetic imaging of microstrip-excited spin waves using electron spins in diamond. a) Idea of the experiment. An ensemble of nitrogen-vacancy (NV) centers in a diamond chip is used to image the magnetic stray fields generated by spin waves in a YIG thin film. The ability to image spin waves underneath metals is used to study the metal-induced spin-wave damping. b–d) Spatial maps of the NV electron spin resonance (ESR) contrast when exciting spin waves resonant with an NV ESR transition. The oscillations result from the interference of the spin-wave and direct microstrip fields. The magnetization (***M***) points along *z*. The directions of the predominantly excited spin-wave vectors (***k***) are indicated. Scale bars: 20 μm. b) Backward-volume spin waves (***k*** ∥ ***M***), excited by applying a drive frequency $\omega/2\pi = 1.934$ GHz that is 0.17 GHz below the FMR at $B_0 = 33.5$ mT. Inset: micrograph of the sample (scale bar: 40 μm). c) Spin waves in the Damon–Eshbach configuration (***k***⊥***M***) excited by applying a drive frequency $\omega/2\pi = 2.590$ GHz that is 1.12 GHz above the FMR at $B_0 = 15$ mT. d) Spin waves underneath and next to a gold microstrip used for spin-wave excitation (inset). Scale bars: 20 μm. As the skin depth of a 2.5 GHz magnetic field in gold is ∼1.6 μm, spin waves are clearly visible underneath the 200 nm gold film.

eddy-current-induced damping mechanism dominates up to a threshold frequency above which three-magnon scattering becomes allowed and increases damping further.

Our imaging platform is an ensemble of shallowly implanted nitrogen-vacancy (NV) centers in diamond (**Figure 1**a). NV centers are lattice defects with an $S = 1$ electron spin that can be polarized by optical excitation, controlled by microwaves, and read out through spin-dependent photoluminescence.[12,13] Since NV centers can exist within ∼10 nm from the surface of diamond,[14] they can be brought within close proximity to a material of interest. Combined with an excellent sensitivity to magnetic fields,[13] these properties make NV spins well suited for stray-field probing of spins and currents in condensed matter systems.[15]

2. Results

To image propagating spin waves, we place a diamond membrane containing a layer of NV centers implanted ∼10–20 nm below the diamond surface onto a YIG film equipped with 200-nm-thick gold microstrips (Experimental Section). Passing a microwave current through a microstrip generates a magnetic field that excites spin waves in the YIG (Figure 1a). These waves create a magnetic stray field that interferes with the direct microstrip field, leading to a spatial standing-wave pattern in the total amplitude of the oscillating magnetic field.[11] We spatially map this amplitude by locally measuring the contrast of the NV electron spin resonance (ESR) transitions. By changing the drive frequency while adjusting the static magnetic field applied along the NV axis (B_0) to maintain resonance with the NV ESR frequency (Experimental Section), we can excite and detect spin waves with wave vectors either along or perpendicular to the static magnetization *M* (Figure 1b,c). The spin waves are clearly visible both underneath and next to the gold microstrips (Figure 1b–d).

To characterize the metal-induced spin-wave damping, we start by analyzing the spatial spin-wave profiles underneath and next to a gold microstrip that we use to excite spin waves (**Figure 2**a). We select a section of microstrip that is far away from corners (>100 μm) to avoid edge effects. We apply a static magnetic field with in-plane component along the microstrip direction and a drive frequency between 100 and 600 MHz above the ferromagnetic resonance (FMR), resulting in directional spin-wave emission with a large (small) spin-wave amplitude to the right (left) of the microstrip (Figure 2a). This directionality is characteristic of microstrip-driven spin waves traveling perpendicularly to the magnetization and is a result of the handedness of the microstrip drive field and the precessional motion of the spins in the magnet.[16,17] We spatially quantify the amplitude of the local microwave magnetic field generated by the spin

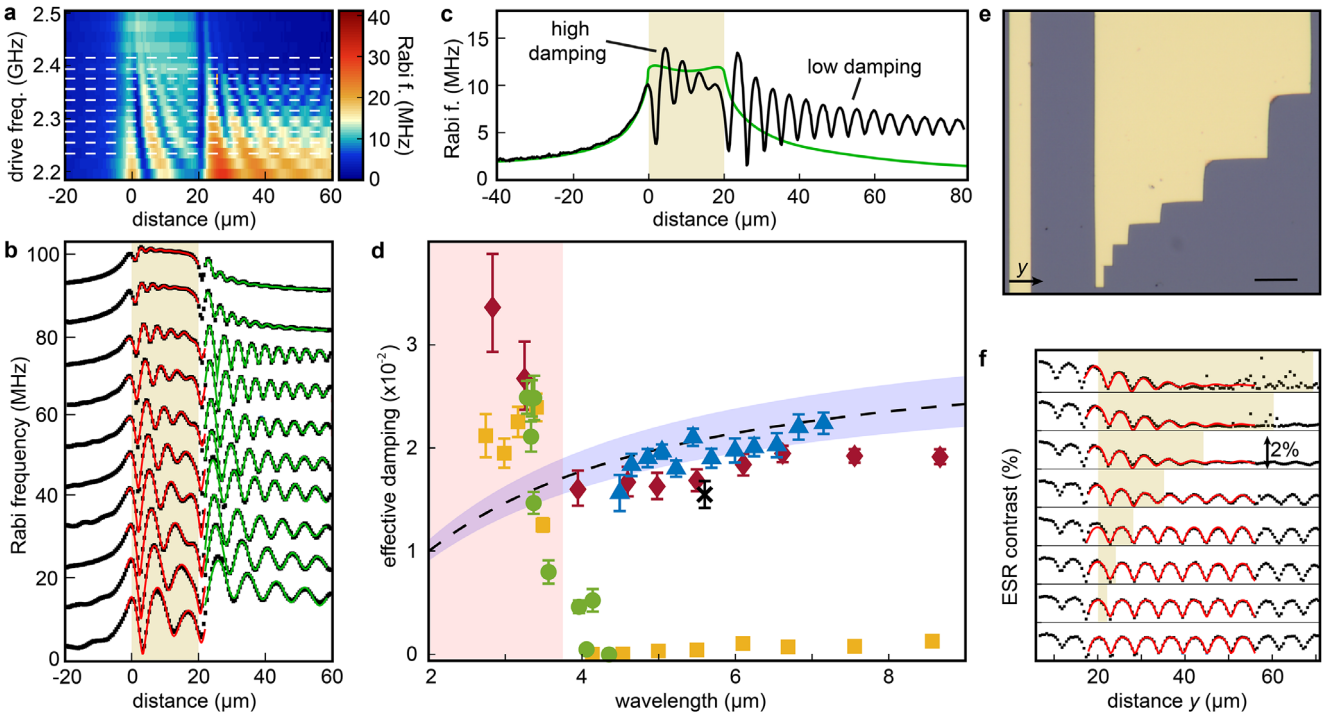

Figure 2. Characterizing metal-induced spin-wave damping. a) Imaging spin waves underneath and next to a gold microstrip located between 0 and 20 μm versus drive frequency. Color scale: measured NV Rabi frequency. b) Linecuts along dashed lines in (a). Black squares: data. Dashed red (green) lines: fits in (next to) the microstrip region. Traces offset by 10 MHz for clarity. c) Measured NV Rabi frequency (black line) and calculated contribution to it from the direct microstrip field (green line) at drive frequency 2.361 GHz, $B_0 = 18.2$ mT. d) Extracted spin-wave damping versus spin-wavelength for different devices. Yellow squares (red diamonds): device in (a,b), next to (under) the microstrip. Black cross: data from (e,f). Blue triangles: wavelength-dependent damping underneath gold structure (Figure 2e; Figure S2, Supporting Information). Green circles: data from Figure 3. Error bars: ±1 s.d. fit uncertainty. Dashed black line: theoretical model (Equation (1)) with shaded purple area indicating 10% uncertainty in gold resistivity. Shaded red area: three-magnon scattering region. e) Image of microstrip and gold structure used in (f). Scale bar: 10 μm. f) ESR contrast along sections of varying length of the gold structure in (e). For each trace, the shaded yellow area indicates the gold structure length. The right microstrip edge is located at $y = 5$ μm. $B_0 = 20.3$ mT, drive frequency $\omega/2\pi = 2.302$ GHz, spin-wavelength = 5.6(2) μm. Black squares: data (for clarity, each trace is offset by 2%). Red lines: fits to a model that calculates the ESR contrast by summing the microstrip and spin-wave fields (Section S2, Supporting Information).

waves by measuring the rotation rate (Rabi frequency) of the NV spins.[18] The spatial oscillations in the measured NV Rabi frequency result from the interference between the microstrip and spin-wave fields.[11] The spin-wavelength is directly visible from the spatial period of these oscillations. We observe a rapid decay of the oscillations underneath the microstrip (Figure 2b), even though the microstrip field is approximately constant in this region (Figure 2c). We can thus conclude that this decay is caused by the decay of the spin-wave amplitude. In contrast, the decrease of the amplitude away from the microstrip follows the decay of the direct microstrip field (Figure 2c).

By fitting the measured spatial decay in- and outside the microstrip region we can extract the additional spin-wave damping caused by the metal. We use a model that calculates the excited magnetization dynamics from the spin-wave susceptibility and the microwave drive current,[11] with the susceptibility depending on the spin-wave damping constant α (Sections S1 and S2, Supporting Information). An accurate description of the measured NV Rabi frequencies (Figure 2a–c) is only possible if we allow for different damping constants in- and outside the microstrip region (see also Figure S1, Supporting Information). We find that the damping underneath the gold microstrip (Figure 2d, red diamonds) exceeds the damping next to the microstrip (yellow squares) by approximately two orders of magnitude.

We argue that the observed strong spin-wave damping underneath the metal is caused by eddy currents that are induced by the oscillating magnetic stray field of the spin waves. Eddy currents have been reported to cause linewidth broadening of ferromagnetic resonances in cavity and stripline-based experiments.[19–25] However, revealing their effect on propagating spin waves, which is important for information transport, has remained an outstanding challenge. We model the effect of the spin-wave-induced currents by including their magnetic field self-consistently into the LLG equation (Sections S1.4 and S1.5, Supporting Information). Doing so, we find that a metal film of thickness t increases the damping to $\alpha = \alpha_G + \alpha_e$, with α_G the intrinsic "Gilbert" damping and

$$\alpha_e = \frac{\gamma \mu_0^2 M_s g^2(k) t h}{4\rho} \frac{(1+\eta)^2}{1+\eta^2} \tag{1}$$

with γ the electron gyromagnetic ratio, μ_0 the vacuum permeability, M_s and h the YIG saturation magnetization and thickness, respectively, k the spin-wavenumber, ρ the metal resistivity, and η the ellipticity of the spin-wave precession. This

expression is derived under the assumption of a homogeneous magnetization across the film thickness t, which becomes strictly valid in the thin-film limit $kt \ll 1$. The form factor $g(k) = (1 - e^{-kh})(1 - e^{-kt})/(k^2th) \approx 1 - k(t + h)$ arises from spatially averaging the dipolar and eddy-current stray fields over the thicknesses of the YIG and metal films. An analysis equating the magnetic energy losses to the power dissipated in the metal yields the same expression (Section S1.7., Supporting Information). We plot Equation 1 in Figure 2d using $\rho = 2.44 \cdot 10^{-8}$ Ω m for the resistivity of gold,[26] finding a good agreement with the damping extracted from the various sets of data without free parameters. The finite width w of the stripline can be disregarded when $kw \gg 1$ (Sections 1.6–1.7, Supporting Information), as is the case in Figure 2d. Accounting for a non-homogeneous magnetization may be achieved via micromagnetic simulations.[16] The damping increase caused by spin pumping is $\alpha_{sp} = \frac{g_s \mu_B}{4\pi M_s} \cdot \frac{g_{\uparrow\downarrow}}{t_{YIG}}$,[27,28] where g_s is the electron Lande factor, μ_B the Bohr magneton, M_s and t_{YIG} the YIG saturation magnetization and thickness, respectively, and $g_{\uparrow\downarrow}$ the YIG/Au spin mixing conductance, with $g_{\uparrow\downarrow} \approx 1 \cdot 10^{18} - 3 \cdot 10^{18} m^{-2}$.[27,28] We may disregard spin pumping since in our samples $4.3 \cdot 10^{-5} < \alpha_{sp} < 1.3 \cdot 10^{-4}$ is ~2 orders of magnitude smaller than the eddy current contribution.

To corroborate the origin of the damping enhancement, we image spin waves propagating underneath a 200-nm-thick gold island deposited next to a microstrip (Figure 2e,f). We observe a progressively decreasing spin-wave amplitude for increasing travel distance under the gold, with an average characteristic decay length of $y_0 = 9(1)$ µm extracted by fitting the top three traces in Figure 2f. We characterize the wavelength dependence by varying the drive frequency (Figure S2, Supporting Information). The corresponding damping values are reported in Figure 2d (black cross and blue triangles) and agree well with Equation 1.

Both in- and outside the stripline region, we observe a sudden increase in damping above a threshold frequency $\omega_T/2\pi \cong 2.39$ GHz (Figure 2a). We further characterize this increase by zooming in to the threshold frequency (**Figure 3**a,b) and extracting the damping parameter as a function of the wavelength (Figure 2d, green circles). For the spin waves outside the microstrip region, the increase occurs in a ~10 MHz frequency range of the order of the intrinsic spin-wave linewidth.

The spin-wave dispersion of our YIG films (Section S1.3, Supporting Information) explains the observed increase in damping above ω_T in terms of three-magnon scattering – a momentum- and energy-conserving process in which a magnon decays into two of half its frequency (Figure 3c).[29] This process becomes allowed only above a threshold drive frequency ω_T such that $\omega_T/2$ exceeds the bottom of the spin-wave band (ω_{min}) (Figure 3c; Figure S3, Supporting Information). The additional scattering increases the spin wave damping and decreases its decay length. The onset of three-magnon scattering was previously identified using Brillouin light scattering.[30] Our real-space imaging approach reveals its dramatic effect on the spatial spin-wave decay length important for spin-wave transport. These measurements highlight that damping caused by three-magnon scattering limits the frequency range within which coherent spin waves in YIG thin films can serve as low-damping carriers to $\omega_{min} < \omega < 2\omega_{min}$.

Finally, we demonstrate that the ability to study spin waves underneath metals also enables the detection of hidden spin-wave scattering centers, highlighting the applicability of this approach for assessing the quality of buried magnetic films in multilayer systems. As an example, we show the scattering patterns produced by defects underneath the metal electrodes used for spin-wave excitation (**Figure 4**a,b). The defects produce characteristic v-shaped patterns, resulting from preferential scattering into the "caustic" directions that are associated with the anisotropic dispersion,[31] making the source of these spin-wave beams clearly identifiable. NV-based spin-wave imaging could therefore be used as a diagnostic tool for magnetic quality, even when the material of interest is buried under metallic layers in a heterostructure.

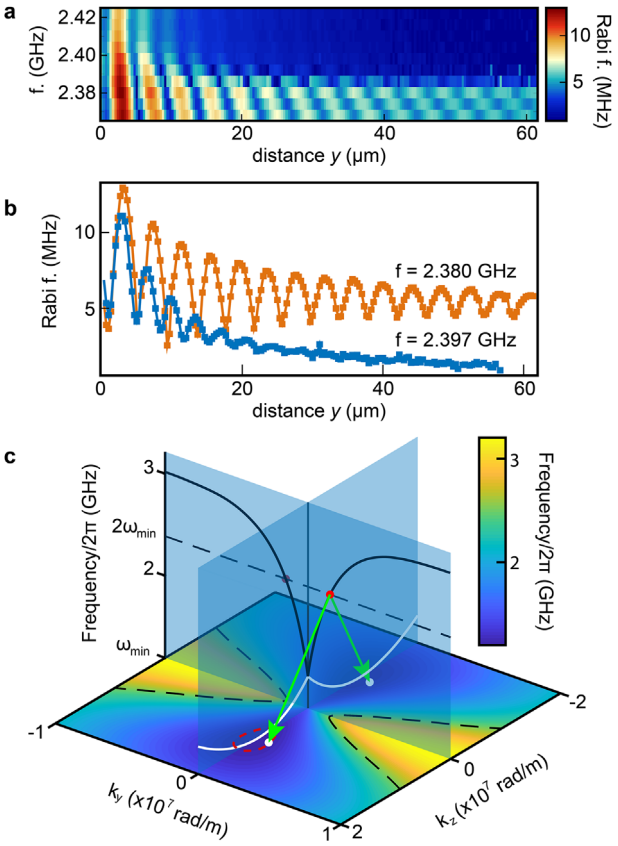

Figure 3. Spatial decay of propagating spin waves caused by three-magnon scattering. a) NV Rabi frequency versus spin-wave drive frequency and distance from the edge of the microstrip used for spin-wave excitation. Above a threshold frequency $\omega_T/2\pi = 2.39$ GHz, the spin-wave damping increases strongly. b) Linecuts of (a) below and above the threshold frequency. When the driving is below the threshold frequency (orange squares and curve), the decrease of the oscillation amplitude follows the decrease of the microstrip field. Above the threshold frequency (blue squares and curve), the spin-wave propagation distance is strongly reduced. c) Calculated spin-wave dispersion for our 235 nm YIG film. The solid black and white lines show the dispersion along the y and z directions, respectively. The microwave drive excites spin waves propagating along y (red dot, Damon–Eshbach configuration). Above the threshold frequency ($\omega_T = 2\omega_{min}$), scattering of one magnon in this mode into two backward-volume magnons (along z, white dots) near the band minimum becomes allowed (red dashed line corresponds to 20 MHz above ω_{min}).

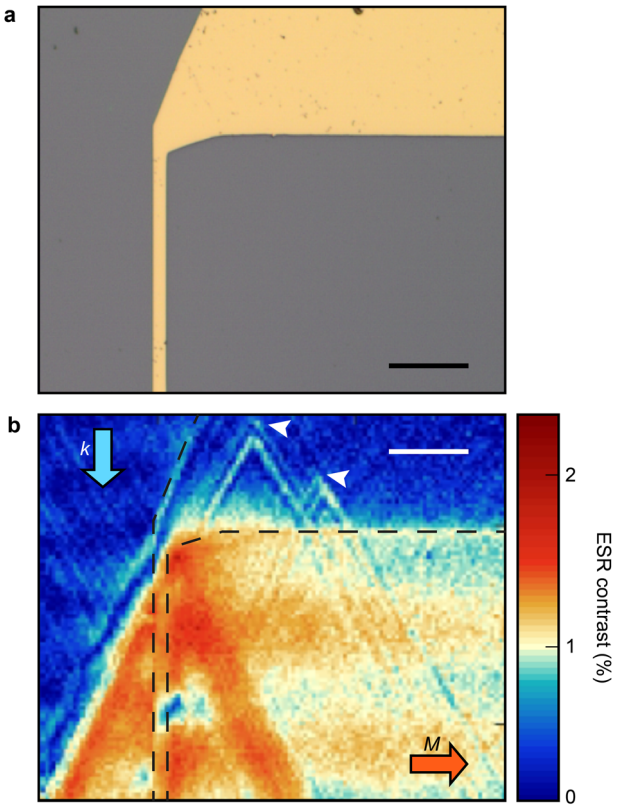

Figure 4. Imaging defect-induced spin-wave scattering underneath a 200 nm metal film. a) Image of the gold microstrip used in (b). Scale bar: 20 µm. b) Spatial maps of the NV ESR contrast for $B_0 = 27.5$ mT and drive frequency $\omega/2\pi = 2.099$ GHz. Two scattering centers (white arrows) are located near the top edge of the image (not clearly identifiable from (a)), as deduced by the scattered caustic beams. Dashed black line: edge of the gold structure. The directions of the magnetization (***M***) and the predominant wavevector (***k***) excited by the microstrip are indicated. Scale bar: 20 µm.

3. Conclusion

In conclusion, we characterized the damping enhancement of spin waves that propagate under metallic electrodes used for spin-wave control, and showed that the increase is well explained by a model that introduces the spin-wave-induced currents into the LLG equation. The ability to detect spin waves underneath metals opens up several exciting new possibilities for studying the interaction between metals and magnets. One example is studying the spectral properties of temperature- or chemical-potential-driven magnon condensates underneath gates in magnon transistors.[8,32,33] Additionally, varying the thickness of the metal and/or magnetic films, or using spacer layers, enables a characterization of interfacial effects such as damping and antidamping of magnons controlled by the spin-Hall effect in heavy metal electrodes.[34] Furthermore, characterizing the screening of the spin-wave stray fields by a metal enables measuring its magnetic susceptibility at well-defined wavenumbers and extracting material parameters such as skin depth, conductivity, and permeability. Finally, the ability to reveal buried scattering centers provides a new tool for assessing the quality of magnetic interfaces and spin-wave devices.

4. Experimental Section

Sample Fabrication: The diamond chip used in this work measured 2 × 2 × 0.05-mm^3 and had an estimated NV density of 10^3 µm^{-2} created via ion implantation at a depth of ∼10–20 nm below the diamond surface (fabrication details in[11]). The YIG film was 235-nm-thick, grown on a 500-µm-thick GGG substrate via liquid phase epitaxy (Matesy gmbh). The saturation magnetization was previously measured[11] to be $M_s = 1.42 \cdot 10^5$ A m^{-1}. To mount the NV-diamond, a drop of isopropanol was deposited onto the YIG and the diamond was placed on top with the NV-surface facing down, while gently pressing down until the IPA has evaporated. The resulting diamond-YIG distance was limited by small particles (e.g., dust). An NV-YIG distance of 1.6(1) µm was extracted from the measured maps of the NV Rabi oscillations.

NV-Based Imaging of Spin Waves: NV centers are optically addressed using a home-built confocal microscope with a 515 nm laser, an NA = 0.95 objective for laser focusing/photon collection, and an avalanche photodiode for NV photon detection (for details of the setup, see ref. [11]). The ESR transition of the NV centers used in this work for spin-wave imaging is tuned by a magnetic field B_0 according to $\omega = D - \gamma B_0$ where $\gamma/2\pi = 28$ GHz T^{-1} is the electron gyromagnetic ratio and $D/2\pi = 2.87$ GHz is the zero-field splitting. In all experiments in Figures 2–4, the magnetic field is oriented at a 54° angle with respect to the sample-plane normal and with an in-plane projection along the microwave stripline, thus aligning it with one of the four possible crystallographic orientations of the NV centers in the diamond. The fields used in this work are below ∼25 mT, much smaller than the YIG saturation magnetization ($\mu_0 M_s = 178$ mT), therefore the YIG magnetization tilts out of plane by less than 5°.[11] We measure Rabi oscillations by applying a ∼1 µs laser pulse to polarize the NV spins into the $m_s = 0$ state, applying a microwave magnetic field at the NV ESR frequency, and reading out the final spin state through the NV's spin-dependent photoluminescence.[13]

Supporting Information

Supporting Information is available from the Wiley Online Library or from the author.

Acknowledgements

This work was supported by the Dutch Research Council (NWO) as part of the Frontiers of Nanoscience (NanoFront) program and through the NWO Projectruimte grant 680.91.115 and by the JSPS KAKENHI Grant 19H006450.

Conflict of Interest

The authors declare no conflict of interest.

Authors Contribution

I.B. and T.S. designed the experiment. B.S. prepared the diamond membrane. I.B. realized the NV magnetometry setup, fabricated the sample and performed the measurements. G.E.W.B., T.S., T.Y., and Y.M.B. developed the theoretical model. J.A. commented on the manuscript. I.B. and T.S. analyzed the data and wrote the manuscript with help from all co-authors.

Data Availability Statement

The data that support the findings of this study are openly available in Zenodo at http://doi.org/10.5281/zenodo.4726771, reference number 4726771.

Keywords

diamond, magnetic imaging, magnetic insulators, NV centers, quantum sensing, spin waves, spintronics

Received: July 14, 2021
Revised: September 2, 2021
Published online:

[1] D. D. Stancil, A. Prabhakar, *Spin Waves*, Springer, New York **2009**.
[2] A. V. Chumak, V. I. Vasyuchka, A. A. Serga, B. Hillebrands, *Nat. Phys.* **2015**, *11*, 453.
[3] A. Barman, G. Gubbiotti, S. Ladak, A. O. Adeyeye, M. Krawczyk, J. Gräfe, C. Adelmann, S. Cotofana, A. Naeemi, V. I. Vasyuchka, B. Hillebrands, S. A. Nikitov, H. Yu, D. Grundler, A. Sadovnikov, A. A. Grachev, S. E. Sheshukova, J.-Y. Duquesne, M. Marangolo, C. Gyorgy, W. Porod, V. E. Demidov, S. Urazhdin, S. Demokritov, E. Albisetti, D. Petti, R. Bertacco, H. Schulteiss, V. V. Kruglyak, V. D. Poimanov, A. K. Sahoo, J. Sinha, H. Yang, M. Muenzenberg, T. Moriyama, S. Mizukami, P. Landeros, R. A. Gallardo, G. Carlotti, J.-V. Kim, R. L. Stamps, R. E. Camley, B. Rana, Y. Otani, W. Yu, T. Yu, G. E. W. Bauer, C. H. Back, G. S. Uhrig, O. V. Dobrovolskiy, S. van Dijken, B. Budinska, H. Qin, A. Chumak, A. Khitun, D. E. Nikonov, I. A. Young, B. Zingsem, M. Winklhofer, *J. Phys.: Condens. Matter* **2021**, *33*, 413001.
[4] T. Fischer, M. Kewenig, D. A. Bozhko, A. A. Serga, I. I. Syvorotka, F. Ciubotaru, C. Adelmann, B. Hillebrands, A. V. Chumak, *Appl. Phys. Lett.* **2017**, *110*, 152401.
[5] G. Talmelli, T. Devolder, N. Träger, J. Förster, S. Wintz, M. Weigand, H. Stoll, M. Heyns, G. Schütz, I. P. Radu, J. Gräfe, F. Ciubotaru, C. Adelmann, *Sci. Adv.* **2020**, *6*, eabb4042.
[6] Q. Wang, M. Kewenig, M. Schneider, R. Verba, F. Kohl, B. Heinz, M. Geilen, M. Mohseni, B. Lägel, F. Ciubotaru, C. Adelmann, C. Dubs, S. D. Cotofana, O. V. Dobrovolskiy, T. Brächer, P. Pirro, A. V. Chumak, *Nat. Electron.* **2020**, *3*, 765.
[7] A. V. Chumak, A. A. Serga, B. Hillebrands, *Nat. Commun.* **2014**, *5*, 4700.
[8] L. J. Cornelissen, J. Liu, B. J. van Wees, R. A. Duine, *Phys. Rev. Lett.* **2018**, *120*, 097702.
[9] J. Sinova, S. O. Valenzuela, J. Wunderlich, C. H. Back, T. Jungwirth, *Rev. Mod. Phys.* **2015**, *87*, 1213.
[10] L. J. Cornelissen, J. Liu, R. A. Duine, J. Ben Youssef, B. J. Van Wees, *Nat. Phys.* **2015**, *11*, 1022.
[11] I. Bertelli, J. J. Carmiggelt, T. Yu, B. G. Simon, C. C. Pothoven, G. E. W. Bauer, Y. M. Blanter, J. Aarts, T. van der Sar, *Sci. Adv.* **2020**, *6*, eabd3556.
[12] A. Gruber, A. Dräbenstedt, C. Tietz, L. Fleury, J. Wrachtrup, C. Von Borczyskowski, *Science* **1997**, *276*, 2012.
[13] L. Rondin, J. P. Tetienne, T. Hingant, J. F. Roch, P. Maletinsky, V. Jacques, *Rep. Prog. Phys.* **2014**, *77*, 056503.
[14] T. Rosskopf, A. Dussaux, K. Ohashi, M. Loretz, R. Schirhagl, H. Watanabe, S. Shikata, K. M. Itoh, C. L. Degen, *Phys. Rev. Lett.* **2014**, *112*, 147602.
[15] F. Casola, T. van der Sar, A. Yacoby, *Nat. Rev. Mater.* **2018**, *3*, 17088.
[16] M. Mohseni, R. Verba, T. Brächer, Q. Wang, D. A. Bozhko, B. Hillebrands, P. Pirro, *Phys. Rev. Lett.* **2019**, *122*, 197201.
[17] T. Yu, Y. M. Blanter, G. E. W. Bauer, *Phys. Rev. Lett.* **2019**, *123*, 247202.
[18] P. Andrich, C. F. de las Casas, X. Liu, H. L. Bretscher, J. R. Berman, F. J. Heremans, P. F. Nealey, D. D. Awschalom, *npj Quantum Inf.* **2017**, *3*, 28.
[19] P. Pincus, *Phys. Rev.* **1960**, *118*, 658.
[20] M. Kostylev, *J. Appl. Phys.* **2009**, *106*, 043903.
[21] M. A. W. Schoen, J. M. Shaw, H. T. Nembach, M. Weiler, T. J. Silva, *Phys. Rev. B* **2015**, *92*, 184417.
[22] Y. Li, W. E. Bailey, *Phys. Rev. Lett.* **2016**, *116*, 117602.
[23] M. Kostylev, *J. Appl. Phys.* **2016**, *119*, 013901.
[24] J. W. Rao, S. Kaur, X. L. Fan, D. S. Xue, B. M. Yao, Y. S. Gui, C. M. Hu, *Appl. Phys. Lett.* **2017**, *110*, 262404.
[25] S. A. Bunyaev, R. O. Serha, H. Y. Musiienko-Shmarova, A. J. E. Kreil, P. Frey, D. A. Bozhko, V. I. Vasyuchka, R. V. Verba, M. Kostylev, B. Hillebrands, G. N. Kakazei, A. A. Serga, *Phys. Rev. Appl.* **2020**, *14*, 024094.
[26] J. D. Cutnell, K. W. Johnson, *Physics*, Wiley, Hoboken **1997**.
[27] L. Jin, D. Zhang, H. Zhang, Q. Yang, X. Tang, Z. Zhong, J. Q. Xiao, *J. Appl. Phys.* **2014**, *115*, 17C511.
[28] H. L. Wang, C. H. Du, Y. Pu, R. Adur, P. C. Hammel, F. Y. Yang, *Phys. Rev. Lett.* **2014**, *112*, 197201.
[29] C. Mathieu, V. T. Synogatch, C. E. Patton, *Phys. Rev. B* **2003**, *67*, 104402.
[30] H. Schultheiss, X. Janssens, M. Van Kampen, F. Ciubotaru, S. J. Hermsdoerfer, B. Obry, A. Laraoui, A. A. Serga, L. Lagae, A. N. Slavin, B. Leven, B. Hillebrands, *Phys. Rev. Lett.* **2009**, *103*, 157202.
[31] T. Schneider, A. A. Serga, A. V. Chumak, C. W. Sandweg, S. Trudel, S. Wolff, M. P. Kostylev, V. S. Tiberkevich, A. N. Slavin, B. Hillebrands, *Phys. Rev. Lett.* **2010**, *104*, 197203.
[32] T. Wimmer, M. Althammer, L. Liensberger, N. Vlietstra, S. Geprägs, M. Weiler, R. Gross, H. Huebl, *Phys. Rev. Lett.* **2019**, *123*, 257201.
[33] M. Schneider, T. Brächer, D. Breitbach, V. Lauer, P. Pirro, D. A. Bozhko, H. Y. Musiienko-Shmarova, B. Heinz, Q. Wang, T. Meyer, F. Heussner, S. Keller, E. T. Papaioannou, B. Lägel, T. Löber, C. Dubs, A. N. Slavin, V. S. Tiberkevich, A. A. Serga, B. Hillebrands, A. V. Chumak, *Nat. Nanotechnol.* **2020**, *15*, 457.
[34] G. Wu, Y. Cheng, S. Guo, F. Yang, D. V. Pelekhov, P. C. Hammel, *Appl. Phys. Lett.* **2021**, *118*, 042403.